Biophysical Journal, Volume 98

Supporting Material

Collision-based Spiral Acceleration in Cardiac Media: Roles of Wavefront Curvature and Excitable Gap

Joseph V. Tranquillo, Nima Badie, Craig Henriquez, and Nenad Bursac

SUPPLEMENTAL MATERIAL

DETAILED MATERIALS & METHODS

Simulations

Computational Models

One-dimensional (1D) cables and two-dimensional (2D) isotropic sheets of homogeneous cardiac tissue were simulated using the monodomain reaction-diffusion equation:

$$\nabla \cdot (\sigma \nabla V_m) = \beta \left[C_m \frac{\partial V_m}{\partial t} + I_{ion} \right] \quad (1)$$

where V_m is the transmembrane voltage, I_{ion} is the total ionic membrane current modeled using the three-variable Fenton-Karma (FK) model (1) or four-variable Fenton model (2), C_m is the membrane capacitance (1 μF/cm^2), σ is the conductivity (1 mS/cm), and β is the ratio of cellular surface area to volume (2000 cm^{-1}). Numerical integration (dx = 0.01cm, dt = 4μs) was performed using a semi-implicit Crank-Nicholson method and forward Euler step. All simulations were run on 16 processors at the Pittsburgh Supercomputing Center and data analyzed using MATLAB (The Mathworks).

The parameter choice for the FK model simulations was motivated by our previous experimental studies in neonatal rat ventricular cardiomyocyte monolayers (3, 4). In particular, the dimensions of the 2D computational tissue domains (2x2 and 3x3 cm^2) were chosen to be similar to those of the rat monolayers. In addition, 16 parameters of the FK model were systematically varied until a Default Parameter Set (DPS, Supplemental Table 1) was obtained to yield "rat-like" action potential duration and conduction velocity restitution properties similar to those measured experimentally. Specifically, the dynamic action potential duration restitution curves had maximum slopes less than one, while action potential duration alternans were absent at all activation rates (4).

Action Potential Duration and Conduction Velocity Restitution

Our previous experimental studies in rat cardiac monolayers (4) indicated that a particular restitution shape associated with a relatively large excitable gap during single spiral activity was necessary for the induction of stable wave multiplication and rate acceleration. To systematically study these phenomena in our computational model, three FK parameters (shaded entries in Supplemental Table 1), namely $\%I_{so}$, the percentage of the slow outward current amplitude relative to the default value, $\tau_{v1,}$ the recovery time constant of the fast inward current, and G_{fi}, the conductance of the fast inward current, were varied independently over a range of values around the DPS defaults in order to capture a broad range of restitution shapes and resulting excitable gaps during single spiral activity. All parameters derived from 1D restitution studies are denoted with a subscript "*r*," and effectively described plane-wave activity.

For each point in space, the activation time was defined at V_m = -30 mV with $dV_m/dt > 0$ and the recovery time was defined at V_m = -70 mV with $dV_m/dt < 0$ (circles in Supplemental Fig. 1 *A*). The cycle length (CL) was defined as the time between two consecutive activations, diastolic interval (DI) as the time between an activation and previous recovery, action potential duration (APD) as the time between an activation and subsequent recovery (Supplemental Fig. 1 *A*), and conduction velocity (CV) as the speed of a propagating activation wavefront.

To construct dynamic APD_r and CV_r restitution curves, six or ten 2× threshold stimuli were applied at one end (x = 0 cm) of a 2 cm cable at each pacing rate (from 1 to 10 Hz in

increments of 0.1 Hz). The CV_r and APD_r of the sixth action potential for the FK model (1) and tenth action potential for the four-variable model (2) at each pacing rate were used to construct dynamic restitution curves. To eliminate boundary effects, APD_r was measured at the center of the cable (x = 1 cm) and CV_r was measured using the difference in activation times at x = 0.5 cm and x = 1.5 cm. APD_r and CV_r restitution curves were constructed by plotting the measured parameters against DI_r (Supplemental Fig. 1 *B*). The minimum diastolic interval (DI_r^{min}) was defined as the smallest DI_r that still yielded propagation for all 6 paced action potentials throughout the 1D cable.

Single and Multi-wave Spirals

A single spiral was initiated in a 2D tissue domain using a cross-field S1-S2 protocol (Supplemental Fig. 1 *C*). For some FK parameter combinations, the wavelength (WL = APD×CV) of a solitary wave was too long for a stable spiral to be induced by the S1-S2 protocol. In these cases, the tissue was preconditioned by a series of plane waves (i.e. line S1 stimuli applied at increasing rates) to effectively reduce the wavelength before the cross-field S2 stimulus was applied. Once a spiral was initiated, ten seconds were allowed to elapse to ensure stable spiral position and rotation rate.

To initiate a multi-wave spiral, a properly timed S3 point stimulus was delivered in the wake of a single spiral wave. The S3 stimulus resulted in wavebreak and the formation of two new waves, eventually yielding one of the following cases: (a) termination of all activity, (b) no change in the number of spiral waves in the tissue, or (c) stable spiral multiplication (Fig. 1). To create different multi-wave spiral patterns, an S3 stimulus was applied either near the tissue boundary to selectively annihilate one of the two newly created waves, or closer to the spiral tip in an attempt to sustain both of the newly created waves. If a stable multi-wave spiral was formed (i.e. persisted for 20 s), an S4 point stimulus was applied in select cases either at the same or a different site in an attempt to further increase the number of stable spirals. FK simulations with greater than two stable spirals were performed in 3x3 cm^2 tissue domains. Similar to our previous experimental studies (4), multi-wave spirals were classified according to the number and chirality of stably rotating spiral waves. For example, a "2/1" multi-wave spiral would have 2 stable spirals of one chirality and 1 of the opposite chirality.

Spiral Data Analysis

2D Maps and Rate Acceleration

For all spiral activities, the same temporal quantities (CL, DI, APD), denoted with a subscript "*s*", were calculated at each point in the 2D tissue using the method outlined above. Time-averaged spatial maps of CL_s, DI_s, and APD_s were created by averaging the obtained values over a minimum of 2 s (~12 cycles) of stable spiral activity. The average temporal excitable gap (TEG) of the single spiral (Supplemental Fig. 1 *B*) was defined as:

$$TEG = DI_{sp} - DI_r^{\min}$$

where DI_{sp} is DI_s averaged at the tissue periphery (2 mm from the tissue boundaries). Since DI_r^{min} was derived from the 1D (plane wave) restitution, the TEG represented an approximate temporal gap relatively far away from the spiral tip (where the spiral wave starts to approximate a plane wave).

The degree of rate acceleration was computed from CL_s averaged at the tissue periphery, $CL_{sp,}$ as:

$$\%Acceleration = \frac{1/CL_{sp}^{Multi-wave} - 1/CL_{sp}^{Single}}{1/CL_{sp}^{Single}} \times 100$$

where CL_{sp}^{Single} and $CL_{sp}^{Multi-wave}$ are the average periods of activation at the tissue periphery during single or multi-wave spiral activity, respectively. The magnitude of the local conduction velocity vector, CV_s, was defined at each node in the tissue as:

$$CV_s = \left|\vec{V}(x,y,t)\right| = \left\|\left[\frac{dx}{dt}, \frac{dy}{dt}\right]\right\| = \left\|\left[\frac{t_x}{t_x^{\,2} + t_y^{\,2}}, \frac{t_y}{t_x^{\,2} + t_y^{\,2}}\right]\right\|,$$

where $t_x = \partial t / \partial x$ and $t_y = \partial t / \partial y$ were both calculated from local activation times of the four neighboring nodes, as previously described (5). Boundary nodes were excluded from this analysis.

Spiral Tip and Arm Dynamics

For all spiral activities, phase maps (Supplemental Fig. 1 *D*) were created using a time-delay embedding technique (3, 6) with a 20 ms time delay. From the phase maps, spiral tips were identified as points where all phases meet. Each tip was tracked in time to obtain tip trajectories, inter-tip distances (for multiple spirals), and spiral tip drift velocities (V_{tip}). The intrinsic spiral tip cycle length, CL_s^i (i.e., the revolution period of a spiral arm around its tip), of each spiral was calculated by defining a phase angle, θ, between the *x*-axis and the vector originating from the spiral tip and ending at the center-of-mass of the activation wavefront between arc distances of 1.5 and 3 mm from the tip. CL_s^i was computed as the average time required for the phase angle to accomplish one full rotation (i.e., for the angle θ to traverse 2π radians, Supplemental Fig. 1 *F*). By calculating V_{tip} and CL_s^i, the effects of spiral tip drift and spiral arm rotation could be studied separately (effectively making the spiral tip stationary).

Wavefront Curvature

Wavefront curvatures at each point in space were calculated using a modification of the Kay and Gray (7) algorithm. Specifically, we defined a *wavefront* at a particular time, *t*, as a set of discrete points (*x,y*) that have activated (i.e., reached -30 mV) and had between one and three neighboring nodes that activated within 10 ms after *t*. Tip coordinates were identified by determining which wavefront node was surrounded by the smallest number of neighboring wavefront nodes. Starting from the tip, a nearest-neighbor search was used to assign an arc length, "*s"* (distance along the wavefront from the tip), to each node on the wavefront.

Parameterization of wavefront nodes as a function of arc length allowed each wavefront to be redefined by a set of discrete, one-to-one functions, *x(s)* and *y(s)*. Cubic splines were fit to *x(s)* and *y(s)* in order to smooth the inherent spatial discreteness of the data. Naturally higher curvatures near spiral tips were captured by reducing the spline least-squares error tolerance within an arc length of 3 mm from the wavefront tip. The resulting parameterized, cubic spline-fitted functions, *X(s)* and *Y(s)*, were used to approximate the curved spiral wavefronts.

The curvature vector, $\vec{K}$, was defined as the derivative of a curve's unit tangent vector, $\vec{T}$.

$$\vec{T}(s) = \left[T_x(s), T_y(s)\right] = \left[\frac{\dot{X}(s)}{\sqrt{\dot{X}(s)^2 + \dot{Y}(s)^2}}, \quad \frac{\dot{Y}(s)}{\sqrt{\dot{X}(s)^2 + \dot{Y}(s)^2}}\right].$$

$$\vec{K}(s) = \frac{d\vec{T}(s)}{ds} = \left[K_x(s),\, K_y(s)\right] = \left[\frac{\ddot{X}(s)\,\dot{Y}(s)^2 - \ddot{Y}(s)\,\dot{X}(s)\,\dot{Y}(s)}{\left(\dot{X}(s)^2 + \dot{Y}(s)^2\right)^{3/2}}, \quad \frac{\ddot{Y}(s)\,\dot{X}(s)^2 - \ddot{X}(s)\,\dot{X}(s)\,\dot{Y}(s)}{\left(\dot{X}(s)^2 + \dot{Y}(s)^2\right)^{3/2}} \right].$$

The curvature vector, $\vec{K}$, points toward the center of the circle locally describing the curve, and has a magnitude equal to the inverse of the circle's radius. The scalar curvature commonly used to describe wavefronts, κ, is equal to the magnitude of the curvature vector and is positive, by convention, if $\vec{K}$ and the local velocity vector, $\vec{V}$, point to opposite sides of the wavefront (i.e., wavefront is convex, Supplemental Fig. 1 *E*) and negative if they point to the same side (i.e., wavefront is concave). Mathematically,

$$\kappa(s) = \left|\vec{K}(s)\right| \cdot sign(\kappa(s)) \qquad \text{where } sign(\kappa(s)) = \begin{cases} +1 & if \quad \angle \vec{V}(s), \vec{K}(s) \ \geq 90° \\ -1 & if \quad \angle \vec{V}(s), \vec{K}(s) \ < 90° \end{cases}$$

Two-dimensional curvature maps were created by first assigning the nearest parameterized curvature vector to each original discrete point (*x(s)*, *y(s)*). As spiral wavefronts constantly change morphology, curvature vectors were updated every 1 ms. The final 2D average curvature map for each tissue was calculated by averaging curvature magnitudes, κ, over at least 3 s of spiral activity.

ΔCV_s Maps

To distinguish the effects of curvature on CV_s (independent of DI_s), we constructed spatial ΔCV_s maps during single and multi-wave spiral activity, as follows. For each location in the tissue and its associated DI, the CV was conceived as being contributed by two terms: (a) the velocity of the plane wavefront at this DI (obtained from the 1D restitution curve), and (b) the perturbation, ΔCV, due to the presence of wavefront curvature, κ, i.e.,

$$CV_s(DI, \kappa) \quad = \quad CV(DI, \kappa = 0) + \Delta CV_s \quad = \quad CV_r(DI) + \Delta CV_s .$$

To construct ΔCV_s maps, each location in the tissue, associated with an average DI_s and average CV_s, was assigned a ΔCV_s value equal to CV_s - $CV_r(DI_s)$. For $\kappa > 0$, a negative ΔCV_s was expected, indicating a slower velocity of the positively curved vs. plane wavefront, while the opposite was expected for $\kappa < 0$. In addition, for all locations with a given curvature, κ, in the tissue, ΔCV_s values were averaged to construct plots of mean ΔCV_s vs. κ.

Parameters of Action Potential Depolarization

ΔCV_s values in selected tissue locations were related to the underlying action potential depolarization by constructing dV_m/dt vs. V_m portraits. These plots were used to assess membrane charging during early action potential depolarization and derive the "take-off potential", V_m^{min}, and maximum upstroke velocity, $(dV_m/dt)^{max}$ (8). The obtained parameters in spiral waves were compared to those of the corresponding plane waves (1D cable) with the same DI.

Tissue Size and the Maintenance of Multi-wave Spirals

In order to test if a relatively small tissue size (3x3 cm^2) is necessary for the maintenance of multi-wave spirals and stable rate acceleration, we either (a) started from a pre-existing, accelerated multi-wave spiral in a 3x3 cm^2 domain and gradually expanded the tissue size to 8x8 cm^2 by adding a 0.25 cm-thick border of resting tissue after every 5 s of spiral activity, or (b) created spirals of the same chirality directly in a 8x8 cm^2 tissue at rest by initiating spiral tips 2 cm apart from one another using methods described by Pertsov at al. (9, 10). The characteristics

of the resulting multi-wave spirals in the 8x8 cm^2 domains were studied after 10 s of stable rotation as described above.

Studies in Human-like Computational Media

To determine the potential applicability of our findings from rat-like computational cardiac media (Fig. 1-6) to native human cardiac tissues, we performed additional simulations in a large 20x20 cm^2 domain using a simplified human-like ventricular model introduced by Bueno-Orovio et al (11). This model was formulated based on a generic four-variable action potential model by Fenton et al. (2) to yield restitution and reentry properties similar to those measured in native human cardiac tissues (11). The original left ventricular epicardial model from (11), with either the default or an increased value of τ_{fi} (0.11 and 0.27, respectively), was studied using the methods described above. An increase in the time constant of the fast inward current, τ_{fi}, in this model corresponds to a reduction of G_{fi} in the three-variable FK model, effectively increasing the excitable gap during single spiral activity (Supplemental Figure 3).

SUPPLEMENTAL MATERIAL REFERENCES

1. Fenton, F., and A. Karma. 1998. Vortex dynamics in three-dimensional continuous myocardium with fiber rotation: Filament instability and fibrillation. Chaos (Woodbury, N.Y 8:20-47.
2. Fenton, F. H., E. M. Cherry, H. M. Hastings, and S. J. Evans. 2002. Multiple mechanisms of spiral wave breakup in a model of cardiac electrical activity. Chaos (Woodbury, N.Y 12:852-892.
3. Bursac, N., F. Aguel, and L. Tung. 2004. Multiarm spirals in a two-dimensional cardiac substrate. Proc Natl Acad Sci U S A 101:15530-15534.
4. Bursac, N., and L. Tung. 2006. Acceleration of functional reentry by rapid pacing in anisotropic cardiac monolayers: Formation of multi-wave functional reentries. Cardiovasc Res 69:381-390.
5. Bayly, P. V., B. H. KenKnight, J. M. Rogers, R. E. Hillsley, R. E. Ideker, and W. M. Smith. 1998. Estimation of conduction velocity vector fields from epicardial mapping data. IEEE transactions on bio-medical engineering 45:563-571.
6. Gray, R. A., A. M. Pertsov, and J. Jalife. 1998. Spatial and temporal organization during cardiac fibrillation. Nature 392:75-78.
7. Kay, M. W., and R. A. Gray. 2005. Measuring curvature and velocity vector fields for waves of cardiac excitation in 2-D media. IEEE transactions on bio-medical engineering 52:50-63.
8. Roth, B. J. 2000. Influence of a perfusing bath on the foot of the cardiac action potential. Circ Res 86:E19-22; discussion E23-18.
9. Zemlin, C. W., K. Mukund, V. N. Biktashev, and A. M. Pertsov. 2006. Dynamics of bound states of same-chirality spiral waves. Phys Rev E Stat Nonlin Soft Matter Phys 74:016207.
10. Ermakova, E. A., A. M. Pertsov, and E. E. Shnol. 1989. On the interaction of vortices in two-dimensional active media. Physica D 40:185-195.
11. Bueno-Orovio, A., E. M. Cherry, and F. H. Fenton. 2008. Minimal model for human ventricular action potentials in tissue. Journal of theoretical biology 253:544-560.

Supplemental Table 1

Parameter	G_{fi}	k	τ_0	τ_r	τ_{si}	τ_{v1}	τ_{v2}	τ_v^+	τ_w^-	τ_w^+	uc	uc_{si}	uc_v	v_{fi}	V_{rest}	I_{so}
Value	1	240	6	40	47	30	59	30	700	2800	0.13	0.85	0.04	15.0	-85	1

Supplemental Table 1. Default parameter set. Shaded entries denote studied parameters.

Supplemental Table 2

Para-meter		1/0 CL (ms)	2/1 CL (ms)	Accel (%)
I_{so}	**0.80**	160	160	0.0
	0.85	160	160	0.0
	1.00	166	166	0.0
	1.20	188	182	3.3
τ_{v1}	**20**	145	142	2.1
	30	166	166	0.0
	60	198	180	10.0
	100	211	179	17.9
G_{fi}	**0.7**	366	313	16.9
	0.8	241	208	15.9
	1.0	166	166	0.0
	3.0	145	145	0.0

Supplemental Table 2. Degree of acceleration. Mean cycle lengths and acceleration of 2/1 spiral for different parameter values.

Supplemental Figure 1

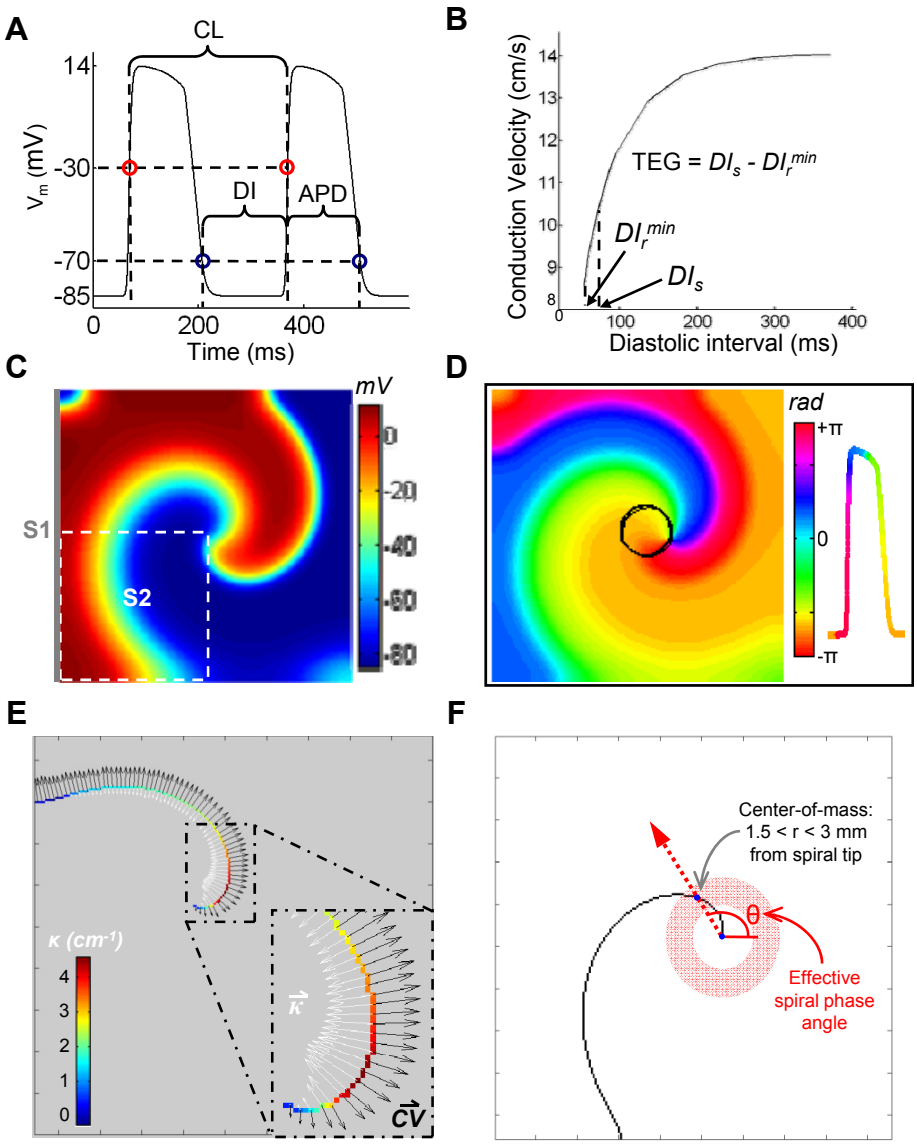

Supplemental Figure 1. Restitution and single spiral analysis shown for the default parameter set (DPS). (*A*) Transmembrane potential corresponding to two stimulated action potentials. Red and blue circles denote activation (-30 mV) and recovery (-70 mV), respectively, and define diastolic interval (DI), action potential duration (APD), and cycle length (CL). (*B*) Conduction velocity (CV) restitution as a function of DI, calculated in a stimulated 1D cable. DI_r^{min} is the minimum DI at which 1:1 propagation fails, DI_s and TEG are respectively the average spiral DI and temporal excitable gap far from the spiral tip. (*C*) Isopotential map of a single spiral in a 2x2 cm^2 tissue domain induced by an S1 line stimulus at the left border (gray line) followed by an area S2 stimulus (white dotted frame). (*D*) Corresponding phase map (in radians) along with the spiral tip trajectory during 600 ms of activity (black line). Purple color corresponds to spiral wavefront (depolarization at -30 mV). (*E*) Spiral wavefront shown with curvature (κ) and conduction velocity vectors. Wavefront pixels and colorbar denote curvature magnitudes. (*F*) Calculation of spiral phase angle, θ, between the *x*-axis and phase vector from spiral tip to the center-of-mass of the arc between 1.5 and 3 mm from tip.

Supplemental Figure 2

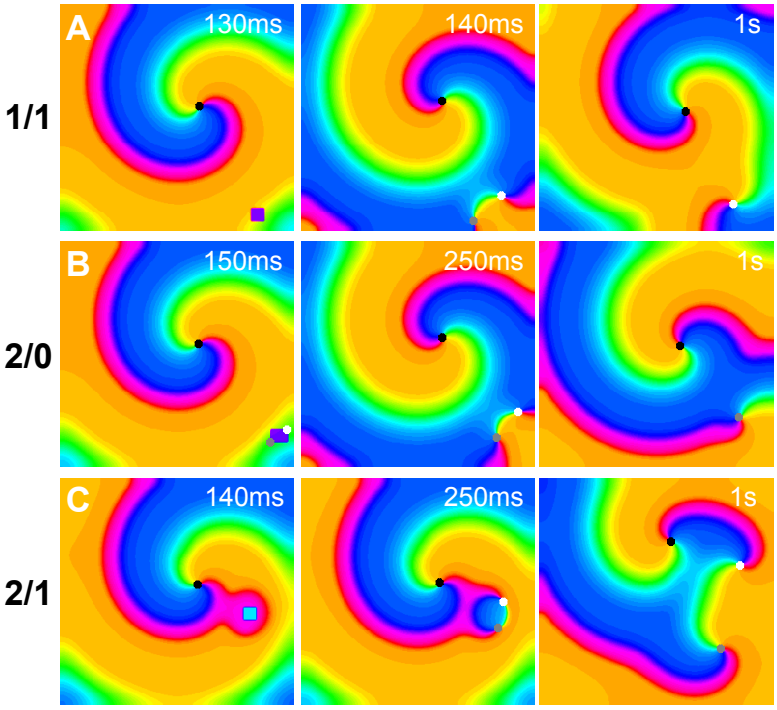

Supplemental Figure 2. Formation of stable multi-wave spirals. Phase snapshots demonstrating a single, properly timed and positioned point stimulus (small square) applied during spiral activity yielding stable wave multiplication. (*A*) Adding a single wave with chirality (direction of rotation) opposite from that of the initial wave yields a 1/1 spiral. (*B*) Adding a single wave with chirality identical to that of the initial wave yields a 2/0 spiral. (*C*) Adding two waves with opposite chiralities yields a 2/1 spiral. White dots denote spiral tips with positive (clock-wise) chirality. Black and gray dots denote spiral tips with negative chirality. All tissue domains have an area of 2x2 cm^2.

Supplemental Figure 3

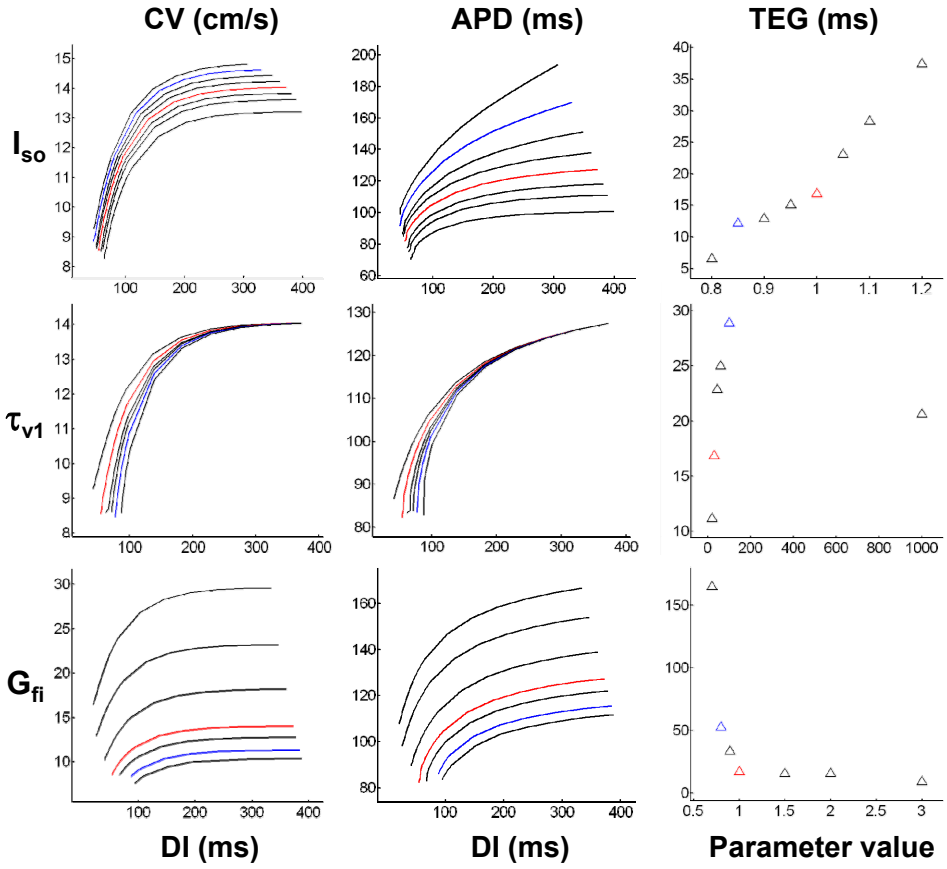

Supplemental Figure 3. Restitution curves and temporal excitable gaps during single spiral activity. Rows show superimposed plots for different values of I_{so} (0.8, 0.85, 0.9, 0.95, 1, 1.05, 1.1, 1.2), τ_{v1} (20, 30, 45, 60, 100, 1000), and G_{fi} (0.7, 0.8, 0.9, 1.0, 1.5, 2.0, 3.0). Red curves represent the default case and blue curves represent cases used for induction and analyses of stable multi-wave spirals. TEG was calculated for 10 s of stable spiral activity.

Supplemental Figure 4

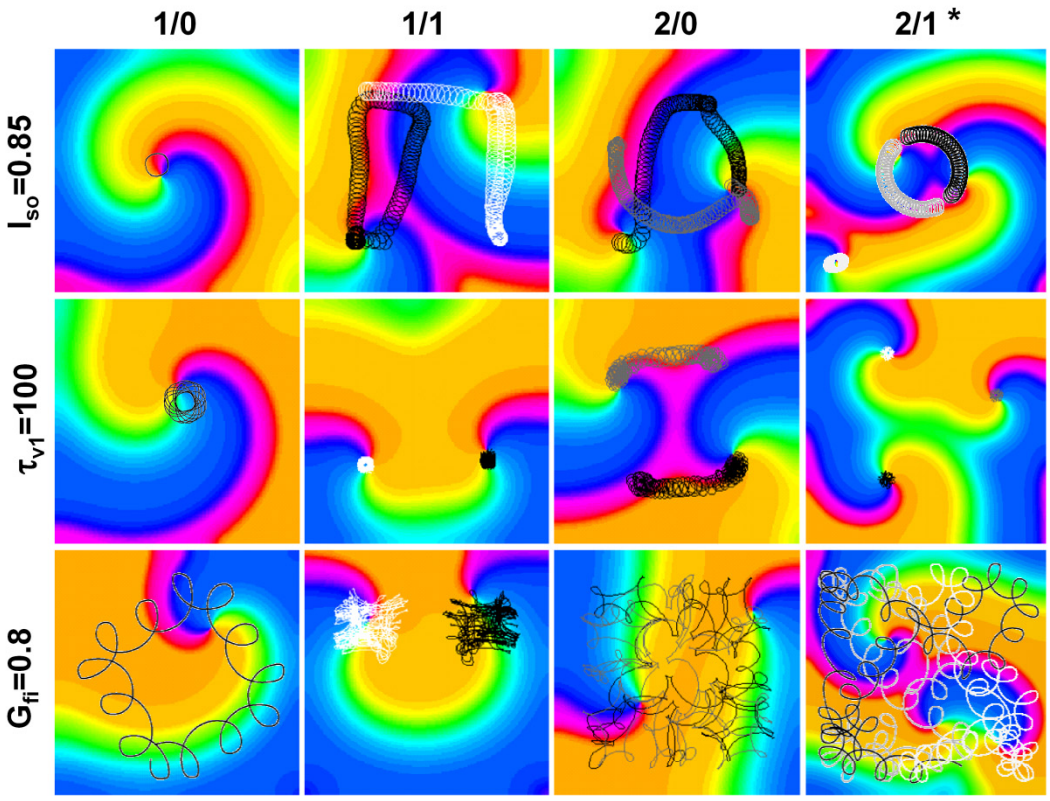

Supplemental Figure 4. Tip trajectory plots of single and multi-wave spirals. Rows contain different spiral types (column titles) obtained for a specific parameter value (shown to the left) with remaining parameters as shown in Supplemental Table 1. Asterisk denotes 3x3 cm^2 tissue domains. All other domains are 2x2 cm^2. Tip trajectories are shown for 10-56 cycles of spiral activity. Single spirals are assigned 1/0 chirality type. Remaining nomenclature is the same as in Supplemental Fig. 2.

Supplemental Figure 5

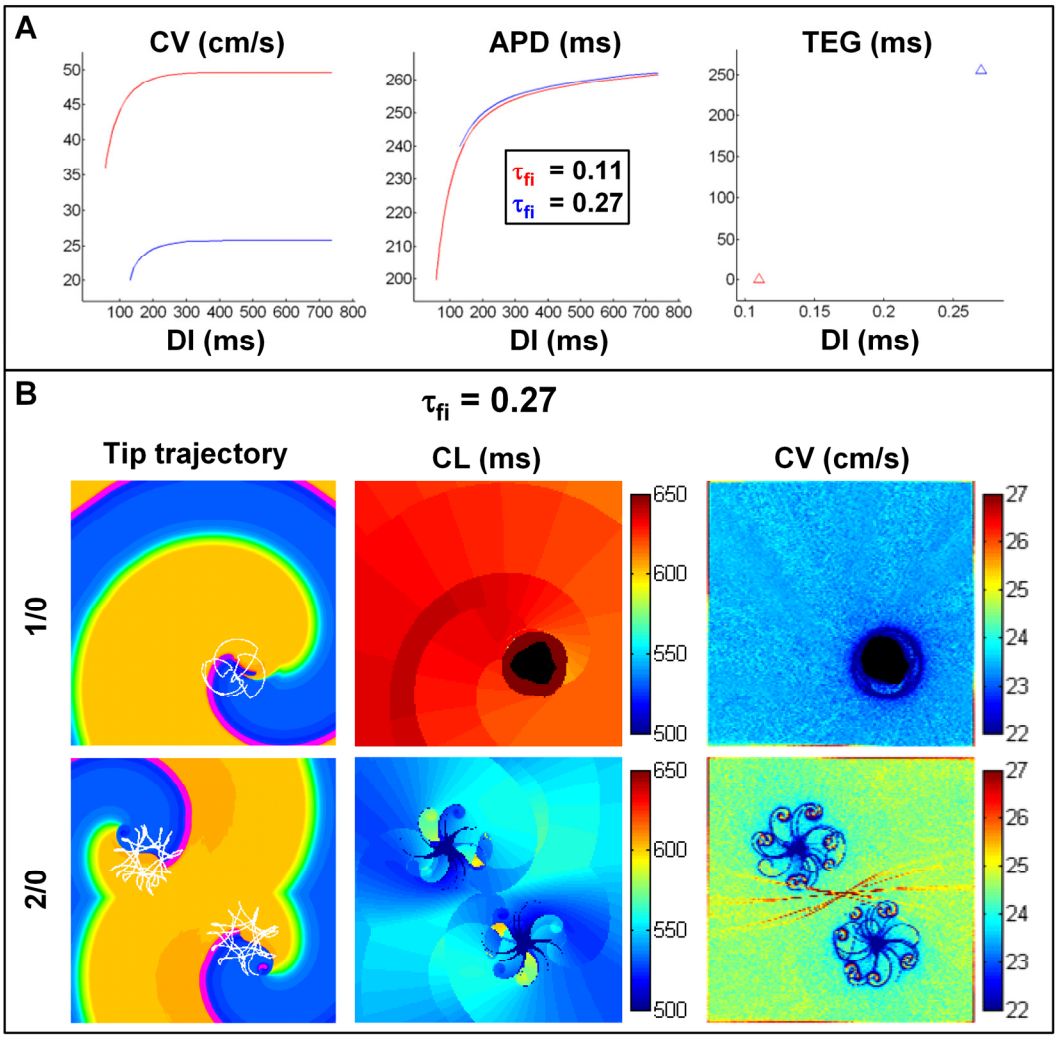

Supplemental Figure 5. Restitutions and spiral acceleration in human-like cardiac media. (*A*) CV and APD restitution curves as a function of DI, calculated in a stimulated 1D cable, and TEG of a single spiral induced in a 20x20 cm^2 medium. Red represents the default case (τ_{fi}=0.11) which resulted in a negligible TEG. Blue represents the modified case (τ_{fi}=0.27) with a significant TEG used for the induction of stable multi-wave spirals. (*B*) Phase maps with spiral tip trajectories (left), CL maps (middle), and CV maps (right) shown in a 20x20 cm^2 medium for the 1/0 and 2/0 spirals. Note that, despite the 15.39% rate acceleration (i.e., reduction in CL_s from 623 to 540 ms) and decrease in DI_s (from 388.6 to 306.9 ms, not shown), the CV_s values in the 2/0 spiral were increased compared to the 1/0 spiral (from 23.5 to 24.6 cm/s), similar to results obtained in smaller media with rat-like properties (Fig. 2 and Table 2).